Research Article | Vol. 29, No. 14 / 5 July 2021 / Optics Express 22688
Optics EXPRESS

Disk-loaded silicon micro-ring resonator for high-*Q* resonance

HOMA ZAREBIDAKI,[1,2] MORTEZA FATHIPOUR,[1] MAHMOUD SHAHABADI,[2,*] AND WIM BOGAERTS[3,4]

[1]*TCAD Laboratory, School of Electrical and Computer Engineering, University of Tehran, Tehran, Iran*
[2]*Photonics Research Laboratory, Center of Excellence on Applied Electromagnetic Systems, School of Electrical and Computer Engineering, College of Engineering, University of Tehran, Tehran, Iran*
[3]*Photonics Research Group, Department of Information Technology, Ghent University-IMEC, Ghent, Belgium*
[4]*Center of Nano-and Biophotonics, Ghent University-IMEC, Ghent, Belgium*
[*]*shahabad@ut.ac.ir*

Abstract: By adding two disks to a standard silicon micro-ring resonator, a very high-quality factor (Q) asymmetric resonance with Q values as high as 7.773×10^5 and slope rates in excess of 880 *dB*/*nm* can be achieved. A circuit model has been proposed for this device based on which an analysis has been carried out that can predict the effect of reflections in the coupling components. Depending on the coupling coefficient between the disks and the micro-ring resonator (MRR), it is possible to use this design in three regimes, with different spectral features. Moreover, it is shown that the disks introduce a discontinuity in the transmission spectrum and the relative positioning of the disks in the ring provides a new degree of freedom in the design step. The proposed device features a high extinction ratio (ER) around 1550 *nm* and could be fabricated in any standard silicon photonics technology without requiring any extra materials or processing steps. The proposed resonator has a high sensitivity of $\Delta\lambda_{Res}$ $(nm)/\Delta n > 299$ *nm*/*RIU*, which makes it suitable for sensing applications and efficient modulators.

1. Introduction

Recent advances in optical signal processing show promise to overcome the speed limitations imposed by electronics, to provide functions much needed in future high capacity communication networks [1,2]. Because of their compact footprint, excellent wavelength selectivity and high-quality factor (Q), micro-ring resonators (MRR), in particular those implemented in silicon photonics, have proven themselves to be very versatile building blocks [3–5]. They are used in filters [4,6], low-power switches and modulators [7–11], ultra-small laser cavities [12] as well as chemical and inertial high-efficiency sensors [13,14] relying on availability of high-Q MRR [15].

The bandwidth-power trade-off in silicon resonant optical modulators and switches limits the modulation efficiency of ring resonator devices. In order to overcome this limitation, an asymmetric line shape resonance (Fano-like) was used [2,11,16,17]. Such an asymmetric spectrum with a very high slope rate (of the transmission as a function of wavelength) lends itself for ultra-high sensitive sensors [18]. To implement a high-Q asymmetric resonance in an MRR, some modifications to the ring geometry such as coupling the ring to additional resonant or realization of interferometric modes are required. This demands careful design or additional fabrication steps. For instance, to couple forward and backward propagating ring modes, one can utilize a grating-based Fabry-Perot cavity [19], implement a grating-assisted silicon MRR [20] or introduce a small air-hole in the bus-waveguide [21].

In this paper, we demonstrate a modified MRR by incorporating two small disk resonators that act as a discontinuity, in order to generate a high-Q resonance. In this fashion, a high-Q resonance mode of the disk is coupled to one of the resonance modes of the MRR. Because of the

#430268 https://doi.org/10.1364/OE.430268
Journal © 2021 Received 29 Apr 2021; revised 14 Jun 2021; accepted 20 Jun 2021; published 2 Jul 2021

Optics EXPRESS

efficient coupling between a continuous background and a discrete resonant mode, an asymmetric (Fano-like) resonance is realized with an extremely sharp slope. To model the behavior of this disk-loaded MRR, we develop an efficient circuit model which also includes unintentional effects caused by the reflections in the couplers into account. The parameters used in this analysis are extracted directly from measurements on a fabricated device. One of the advantages of the proposed ring resonator architecture is its simplicity and small footprint. Moreover, it is compatible with most standard sub-micrometer silicon-on-insulator (SOI) processes that can be executed in a complementary metal-oxide semiconductor (CMOS) fab. Thus, it provides a route for low-cost, large-scale manufacturing and integration with other circuit functions. In terms of performance, the device exhibits an extinction ratio (ER) >15 dB, a slope rate higher than 800 dB/nm and a full width at half maximum (FWHM) of 2×10^{-3} nm, leading to a Q value of about 8×10^5, which to the best of our knowledge, is the largest value reported for an all-silicon MRR of such small dimensions, fabricated by standard passive photonic integrated circuit (PIC) fabrication process [13–15,20]. In this design, it is also possible to achieve high values of ER and Q simultaneously, by adding a phase shifter on the MRR and tuning the refractive index of the disks (e.g. using a heater or by illuminating the disk). Therefore, the structure can easily be tailored for the applications in which a high-Q resonance with large ER is required, such as modulators [16] and sensors [13,18].

2. Disk-loaded micro-ring resonator

2.1. Schematic of the disk-loaded micro-ring resonator

Introducing reflection centers in a MRR provides an effective means to enhance the MRR performance [22–25]. A small reflective discontinuity added to the MRR, couples the clockwise (CW) and counterclockwise (CCW) propagating modes. As a consequence, the resonance in the output spectra will split [23,24,26]. Thus, the resonance shapes can be tuned into a high-Q resonance through control and tailoring of the strength and phase of multiple reflectors.

We have utilized a simple and easy-to-fabricate silicon disk structure which introduces a new coupled resonance. It enhances and controls the inside reflection of the main MRR as well. Figure 1 shows a schematic diagram for the proposed disk-loaded MRR device and is further discussed in section 3. We denote the main MRR radius by r_{Ring}, the coupling distance between the waveguide of the MRR and the bus by d_1 while d_2 is the distance between the MRR waveguide and the disk edge. The coupling and transmission coefficient of the coupler I (i.e., bus waveguide(s) to MRR) are represented by κ_{Ring} and τ_{Ring}, respectively. The radius of each disk is r_{Disk} and the coupling and transmission coefficient of the coupler II (MRR to disk(s)) are κ_{Disk} and τ_{Disk}, respectively. θ_1 is the angle between the MRR diagonal perpendicular to the bus waveguide and the MRR diagonal going through the center of the upper disk. Similarly, the positional angle θ_3 indicates the angular offset of the lower disk. Note that the radius and angles here correspond to the abstract representation of a perfectly circular ring. In the practical implementation a rounded rectangle shape is used for the ring path, and the angles indicate the relative position along the circumference of the ring.

In the designed structure presented further, all waveguides are considered to be air-clad silicon strips fabricated on a standard SOI substrate. The design allows for device fabrication using standard passive silicon CMOS manufacturing technology, where the disks too, are made of silicon. The design can be implemented with oxide cladding, prevalent in most industrial silicon photonics processes.

2.2. Circuit-model analysis for the resonator

To predict the device characteristics and explore the impact of each of its parameters on device performance, a simple, fast and accurate model is needed. For the design with two disks

Optics EXPRESS

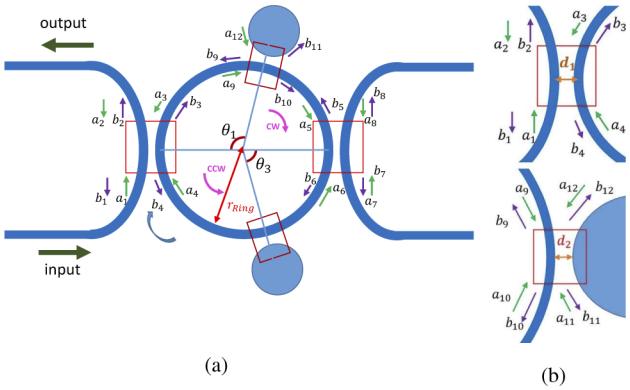

Fig. 1. (a) Proposed disk-loaded ring resonator. The angles θ_1 and θ_3 are the angles that the first and second loading disks make with the horizontal diameter of the MRR. In a non-circular ring, these angles denote the relative position along the circumference of the ring. (b) Definition of coupling coefficients from waveguide to the MRR and from MRR to disk, d_1 is the distance between the bus waveguide and the MRR waveguide, d_2 is the distance between the MRR waveguide and the disk edge.

coupled to an MRR, presented here, the back-reflection from the coupling sections cannot be neglected. Generally, analysis of cascaded MRRs is carried out with one of the two methods: (i) the conversion of the scattering matrices to transfer matrices [27], or (ii) applying signal-flow graph analysis [28]. However, reflection is usually not included in any of the above methods. Furthermore, the couplers are considered as simple two-port networks. Ctyroky, *et al.* [29] studied a simple single MRR taking the reflection effect into account. They used a full 4×4 scattering matrix for each element. Their model showed excellent agreement with FDTD numerical results.

In order to develop a circuit-level model, we approximate the optical component with a black box and model each passive, linear photonic component by a simple scattering matrix (S-matrix) between the input and output ports [30]. In order to consider reflections, we utilize a full 4×4 scattering matrix for each element, following [29]. Next, we apply the connection matrices in order to connect all of the S-matrices and to obtain the transfer matrix [31]. The matrix for each element is discussed below:

For the loss-less coupler, the S-matrix is unitary. When reflections from the couplers are considered, matrix elements in the 4×4 S-matrix may assume non-zero values [29]. A schematic view of a coupler is depicted in Fig. 2. Reflection from the ports of the bus waveguide is denoted by r_W and reflection from the ports connected to the MRR is represented by r_R. Thus, $S_{11} = S_{22} = r_W$ and $S_{33} = S_{44} = r_R$. For non-ideal couplers, the power in the isolation port is not zero. The backward-coupling coefficients from the MRR waveguide to the bus waveguides $S_{14} = S_{23} = \sigma_{RW}$, and because of reciprocity, the backward coupling from the bus waveguides to the MRR waveguides is also $S_{32} = S_{41} = \sigma_{RW}$. The forward cross-coupling between the busses and the MRR is described by $S_{13} = S_{24} = S_{31} = S_{42} = \kappa_{Ring}$ and the forward self-coupling is described by $S_{12} = S_{21} = S_{34} = S_{43} = \tau_{Ring}$. Thus, the coupler S-matrix, $M_{couplerI}$, becomes:

$$\begin{bmatrix} b_1 \\ b_2 \\ b_3 \\ b_4 \end{bmatrix} = \begin{bmatrix} r_W & \tau_{Ring} & \kappa_{Ring} & \sigma_{RW} \\ \tau_{Ring} & r_W & \sigma_{RW} & \kappa_{Ring} \\ \kappa_{Ring} & \sigma_{RW} & r_R & \tau_{Ring} \\ \sigma_{RW} & \kappa_{Ring} & \tau_{Ring} & r_R \end{bmatrix} \begin{bmatrix} a_1 \\ a_2 \\ a_3 \\ a_4 \end{bmatrix} \tag{1}$$

Optics EXPRESS

For a typical MRR, when losses can be neglected and the strength of back-reflection in the coupler, δ, is small ($|r|^2 + |\sigma|^2 = \delta^2 << 1$), we have [29]:

$$\kappa = j\sqrt{1 - \tau^2 - |r|^2 - |\sigma|^2}, \tau = \sqrt{1 - |\kappa|^2 - |r|^2 - |\sigma|^2} \tag{2}$$

The same model can be used for the coupling section II between the MRR and each disk. For the case of coupler at hand, the reflection of the MRR is assumed to be r_R and that from the ports to the disk is represented by r_D. Backward-coupling coefficients from the disk to the MRR waveguide or from the MRR waveguide to the disk is denoted by σ_{RD}.

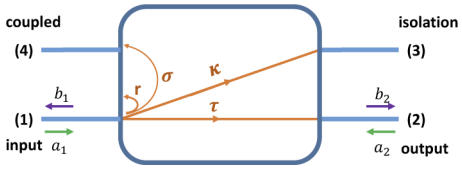

Fig. 2. Schematic of a coupler and definition of relevant symbols

We model the ring waveguide by a simple delay line. For example, $a_9 = b_3 exp(j\beta_{Ring} l_1)$, where $\beta_{Ring} = 2\pi n_{eff}/\lambda$ is the propagation constant of the MRR waveguide and n_{eff} denotes the effective refractive index of the MRR waveguide. In addition, l_1 is the distance (along the ring path) between couplers I and II; $l_1 = r_{Ring}\theta_1$.

The disks are also modeled as rings, but with a higher effective index. In the model, we ignore the excitation of the Whispering Gallery modes of the disks with a higher radial order. If the disk operates in the weak-coupling regime (see section 4.1.2) only a small fraction of optical wave is coupled from the MRR to the disks. This assumption is plausible and fits the measurement data when $d_2 = 300\ nm$ (see section 5.2).

In order to calculate the output/input power transmission spectrum, the scattering-transfer-matrix method, STMM, is utilized [27]. The transfer-matrix, TM, of this structure is:

$$\begin{bmatrix} a_7 \\ b_7 \\ a_8 \\ b_8 \end{bmatrix} = \begin{bmatrix} T_{11} & T_{12} & T_{13} & T_{14} \\ T_{21} & T_{22} & T_{23} & T_{24} \\ T_{31} & T_{32} & T_{33} & T_{34} \\ T_{41} & T_{42} & T_{43} & T_{44} \end{bmatrix} \begin{bmatrix} a_1 \\ b_1 \\ a_2 \\ b_2 \end{bmatrix} \tag{3}$$

TM is calculated as:

$$TM_{4\times4} = M_B \cdot M_{\phi_2} \cdot M_{Disk} \cdot M_{\phi_1} \cdot M_F \tag{4}$$

where M_{ϕ_i} is the connection matrix connecting coupler I to coupler II and accounts for the effects of the light waves traveling in the MRR. It is represented as:

$$M_{\phi_i} = \begin{bmatrix} exp(-j\phi_m) & 0 & 0 & 0 \\ 0 & exp(j\phi_m) & 0 & 0 \\ 0 & 0 & exp(j\phi_n) & 0 \\ 0 & 0 & 0 & exp(-j\phi_n) \end{bmatrix}; \quad \begin{array}{l} i = 1 : m = 4, n = 1 \\ i = 2 : m = 3, n = 2 \\ \phi_k = \beta_{Ring} l_k \end{array} \tag{5}$$

Optics EXPRESS

M_{Disk} is the matrix which transfers the input ports power of coupler II to its output ports:

$$M_{Disk} = \begin{bmatrix} m_{d_{11}} & m_{d_{12}} & 0 & 0 \\ m_{d_{21}} & m_{d_{22}} & 0 & 0 \\ 0 & 0 & m_{d_{33}} & m_{d_{34}} \\ 0 & 0 & m_{d_{43}} & m_{d_{44}} \end{bmatrix} \tag{6}$$

In Eq. (4), the forward contribution of coupler I is represented by M_F, and its backward (output-to-input) contribution is given by M_B, which means $M_B = M_F^{(-1)}$.

When there is no disk added to the MRR, the input light circulates in the MRR waveguide without any interruption and M_{Disk} is an identity matrix. By coupling one disk to the MRR, there will be a discontinuity in the round trip of the light, and this will lead to several extra sharp resonances appearing in the spectrum. This is due to the interference between the MRR modes and the disk modes. When only the upper disk is coupled to the MRR, the matrix elements of M_{Disk} are: $m_{d_{11}} = m_{d_{22}} = 1$ and $m_{d_{12}} = m_{d_{21}} = 0$. Changing the angular position of the disk, θ_1 in this case, changes M_{ϕ_1} and M_{ϕ_2}. In the ideal case, when there is no reflection in the couplers, M_{Disk} is a diagonal matrix. Therefore, the location of this discontinuity does not influence the overall result, since both M_{ϕ_1} and M_{ϕ_2} are diagonal. Note that all of the M_B and M_F elements can be considered wavelength-independent in a first approximation to study the circuit behavior. When there is a reflection from coupler II, M_{Disk} is not diagonal anymore and $m_{d_{34}}$ and $m_{d_{43}}$ take non-zero values. As expected from Eq. (4), in this case, the variation of θ_1 has significant impact on the overall spectrum of the device. This is further discussed in more details in section 4.2.

The output transmission of the through port (b_2) is obtained as:

$$\frac{I_{output}}{I_{input}} = \frac{-T_{31}T_{22} + T_{32}T_{21}}{-T_{32}T_{23} + T_{33}T_{22}} \tag{7}$$

where T_{ij} is ji^{th} element of the transfer matrix of the overall structure. Equation (7) is easily derived from Eq. (3) by setting input intensity $I_{in} = 1$, and assuming the power in the add port is zero. Also, reflections from the add and drop ports are assumed to be zero. This assumption too, is a viable one, since not only these ports reflect very small power, but also the CCW wave (from the ring) couples only slightly to the bus waveguide.

3. Numerical analysis of the disk-loaded MRR

The model parameters are extracted by fitting the data obtained from the measurement to those obtained by simulation, as further discussed in section 5.2.

We have assumed that the effective radius and the effective index (n) for the circulating disk mode are 9.775 μm and 2.5325 and those of the ring are 47.25 μm and 2.3625, respectively. It is impossible to extract the exact value from such a ring resonator, as there is always an uncertainty on the resonance order. The values that have been selected from the possible effective indices for the MRR and the disk, are the ones closest to the values originally used in the design [32] (see section 5.2). We further assume that $\theta_1 = \theta_3 = \pi/2$.

3.1. Simplified model: no reflection

When light is injected into the input port, there exists only a single circulating mode in CW direction, for an ideal MRR with no inside reflection or backscattering. Figure 3 depicts simulation results for the normalized transmission spectra without reflection. The blue line shows the normalized transmission spectrum of an ideal MRR, the red (green) line shows the cases where one and two disks are coupled to the MRR, respectively. We can clearly see two

Optics EXPRESS

types of resonances in this spectrum, the closely spaced MRR resonances and the widely spaced resonances related to the interaction of the disk and the ring. These side resonances are studied in the following sections. Clearly, when two disks are coupled to the ring, a very sharp, high quality resonance with a Q-factor of 7.773×10^5 appears in the spectrum.

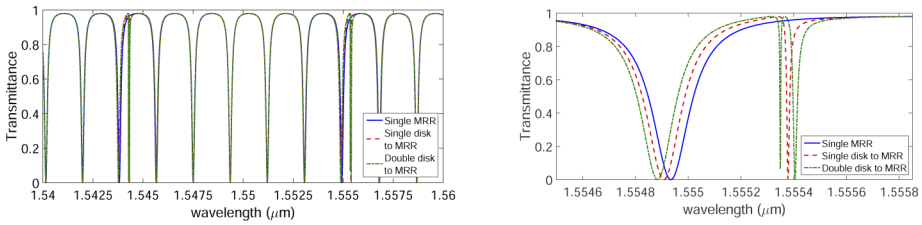

Fig. 3. Comparison of the normalized power transmission, transmittance, spectra for a single ring (blue line), single disk coupled to the MRR (red line) and double disks coupled to the MRR (green line) (a) for 1540 $nm<\lambda<1560$ nm, (b) a zoomed view, delineating the sharpness of the high-Q resonance feature.

The side resonances strongly depend not only on the characteristics of the resonators, but also on the coupling coefficient between the MRR and the disk, i.e., of coupler II. Due to process variability, it is extremely difficult to fabricate an MRR such that all of its coupling factors and losses are matched at any predefined wavelength. Thus, the question may arise as to what are the expected sensitivities of the ER, FWHM and the resonance shape to the coupling coefficient of the MRR and the disk(s), coupler II, when these parameters are varied around the nominal value of the critical coupling coefficient. Table 1 compares the corresponding parameters obtained from numerical simulation studies. It is clear from this table that when the main MRR is coupled to two disks, rather than just one, the resulting resonances become less sensitive to the changes in the coupling coefficient, a property which we will utilize as an advantage in the design.

Table 1. Sensitivities of the parameters of the very sharp resonance (around λ = 1555 *nm*) to the coupling coefficient of coupler II, κ_{Disk}, when one disk and two disks are coupled to the MRR

Ring with	$\Delta E(dB)/\Delta\kappa_{Disk}$	$\Delta FWHM(nm)/\Delta\kappa_{Disk}$
Single Disk	23.458	0.1
Double Disks	14.25	≃0.0

A second advantage of the proposed structure is its tunability. The resonance wavelength shift of the high-Q resonance ($\Delta\lambda_{Res}$) is highly sensitive to the reflective index of the disk (n_{Disk}). If the non-linear effects in the disk material are sufficiently large , n_{Disk} may be varied efficiently by illuminating the disks by a modulating light [33,34]. This is in fact the main motivation for utilization of micro-disk, rather than MRR as the tunable part in the present design. Beside, as a high-speed optical modulator, micro-disk based structures are preferred over MRR-based ones, since they have smaller footprint, less sensitivity to critical dimension variation, larger thermal tuning efficiency and less power consumption [35,36]. Furthermore, this design allows for the modification of optical parameters of the disk(s), including the refractive index, by pumping a controlled amount of light power through the disk(s) with additional waveguides [37]. This is in fact a valuable feature as it facilitates tailoring the resonance features after the device is fabricated. For the double disk structure, we obtain $\Delta\lambda_{Res}(nm)/\Delta n = 299$, while in the case of a single disk, we find $\Delta\lambda_{Res}(nm)/\Delta n = 112$. In this design, it suffices to adjust the refractive index of the disk,

Optics EXPRESS

i.e., a small portion of the entire device, not the index of the entire structure. This feature leads to a more energy efficient switching mechanism with possibly higher modulation/switching speed.

3.2. Analysis of structure considering reflection

Internal reflections will affect the performance of the disk-loaded MRR structure and are important in fabricated optical devices, as already mentioned. In the present design, the coupling sections between the disks and the ring are considered to be the centers of reflections. As depicted in Fig. 4, when a reflection develops inside the MRR, CW and CCW mode are coupled and a new coupled resonance mode is excited, which leads to resonance splitting. Clearly, for all resonances, the ER and FWHM are strongly modified with increasing reflectively. This circuit behaves like a side-coupled integrated spaced sequences of optical resonators (SCISSOR) [38,39] with an infinite number of disks. Light in the ring couples to a disk, the continues around the ring to couple to the disk again, and continues on. The sharpest resonance in the disk is probably a higher radial mode, which does not feel the sidewall so much. Therefore, high-Q resonance is build up in the output spectrum. As this resonance is a result of the interaction of the resonances of the MRR and the disks, a Fano-like shape resonance appears in the spectrum. The characteristics of this resonance can be tailored by modifying the optical path between the couplers, as it has a direct impact on CW and CCW waves. This facilitates achievement of a high-Q resonance which does not suffer from coupler reflection while keeping its ER still high. This feature is studied further in section 4.2.

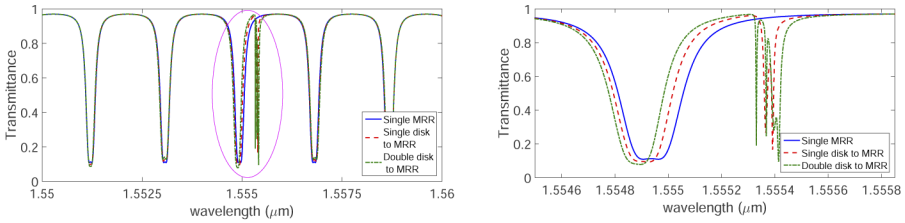

Fig. 4. The power transmittance spectra when reflection is presented, for a single ring (blue line), a single disk (red line) and double disks (green line) coupled to a ring, (a) For 1550 $nm<\lambda<1560$ nm, (b) zoomed view of the sharp resonance.

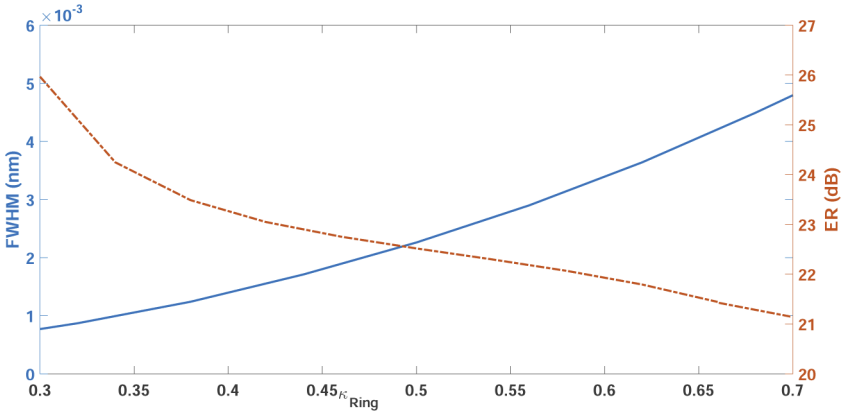

Fig. 5. Variation of the FWHM and ER by changing $|\kappa_{Ring}|$

Optics EXPRESS

4. Tailoring the resonance characteristics

Depending on the targeted application, a design may require stringent constraints on one or another design parameters. In the present design, we aim for a high Q-factor and a very sharp resonance. In this section, we will study how the coupling coefficients impact the shape of the resonance feature and its associated parameters. An interesting parameter in this design is the optical distance between the two disks, which provides an extra degree of freedom for the design. The effect of this parameter is explored in section 4.2.

4.1. Effect of coupling coefficients

We explore the characteristics of the disk-loaded MRR as a function of the coupling between the bus waveguide and the MRR (κ_{Ring}) as well as the coupling between the MRR waveguide and the disks (κ_{Disk}). The coupling ratios are quite sensitive to fabrication, as they are mostly determined by the width of the narrow gap between the waveguides and/or the ring. This study can also be considered as a fabrication tolerance analysis of the disk-loaded MRR under the non-critical-coupling regime [22].

4.1.1. Effect of κ_{Ring}

The high-Q resonance is generated by the interaction of the resonances of the MRR and the disks. As it is clear in Fig. 5, when κ_{Ring} is changed, the ER of the MRR resonance also varies, but the ER of the disk is unaffected. So, the ER of the intended resonance does not change significantly by variation of κ_{Ring}. However, a higher κ_{Ring} makes the MRR resonance wider, and therefore the FWHM of the intended resonance will increase. The variation of FWHM due to changes in κ_{Ring} is 12× less than the same variation for a single MRR with the same dimensions.

4.1.2. Effect of κ_{Disk}

Depending on the coupling coefficient of the MRR and the disks, there are three regimes in the output spectrum of the disk-loaded MRR, as shown in Fig. 6.

Weak-coupling regime In this regime, the coupling strength between the MRR and the disk is less than the damping coefficient of the MRR, γ_{MRR}, where the amplitude of light decays by $(1-\gamma_{MRR})$ at MRR output port. Hence, a Fano resonance with an extremely sharp slope and asymmetric line shape is achievable. For the proposed structure, the resonance of disk acts as a high-Q resonance, while the MRR resonance acts as a low-Q resonance. Therefore, the interference between these two produces an asymmetric Fano resonance with a slope rate higher than 800 dB/nm.

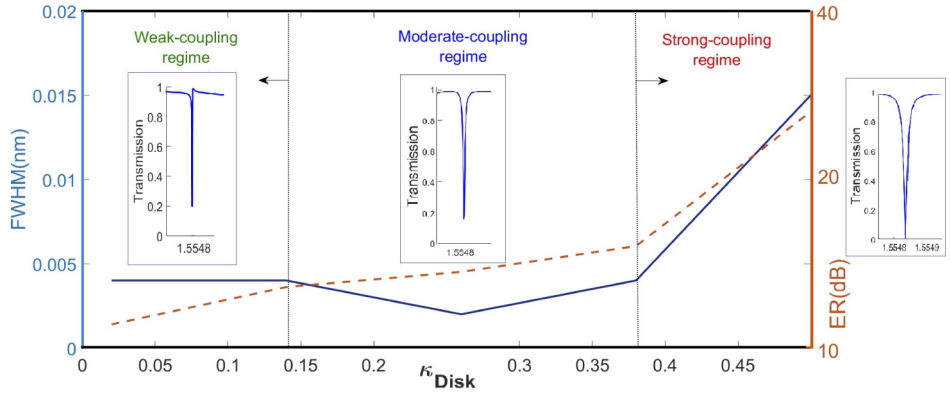

Fig. 6. Variation of the FWHM and ER by changing $|\kappa_{Disk}|$

Optics EXPRESS

In this regime, it would be more efficient to use two small MRRs, with same radius, instead of disks, since a MRRs suffer from lower loss in comparison to a disk.

Moderate-coupling regime The coupling strength between the disk and the MRR is moderate in this regime; this means that the coupling is higher than the difference between the damping coefficients of the disks and MRR, but smaller than their sum ($|\gamma_{MRR} - \gamma_{Disk}| < \kappa_{Disk} < \gamma_{MRR} + \gamma_{Disk}$) [17,40]. The resulting resonance may not be referred to as Fano resonance anymore, but it still has an asymmetric line shape with a small FWHM, providing a high-Q resonance.

In this regime, the strongest response to a perturbation in the disk is observed, with a $\Delta\lambda(nm)/\Delta n$ of about 299 nm, see section 3.1. $\Delta\lambda$ is the shift of the resonance wavelength, while refractive index of each disk is changed by Δn. This high $\Delta\lambda(nm)/\Delta n$ makes the device a perfect candidate for an optically tunable device such as a modulator or a sensor.

Strong-coupling regime When the disks are strongly coupled to the MRR, the resonances of the normalized transmission spectrum split far away from each other and do not interact anymore [40]. The resonance line shape is no longer asymmetric and its FWHM grows wider as the κ_{Disk} is increased and approaches the pure resonances of a disk of the same dimensions.

4.2. Tuning mechanism

In the proposed structure, shown in Fig. 1, the disk-ring couplers function as discontinuities that generate the reflections. Therefore, the relative position of each disk with respect to the MRR center can significantly impact the wavelength response of the structure. The position determines the relative phase of the CCW and CW propagation, and with reflections caused by the two disks, the net reflection can vary between destructive and constructive interference. The normalized transmission spectrum of the device is depicted in Fig. 7. The positional angle of the upper disk (see Fig. 1) is taken as a parameter: ($\theta_1 = \pi/3, \pi/2$ *and* $5\pi/6$), respectively, while θ_3 is kept constant, equal to $\pi/2$.

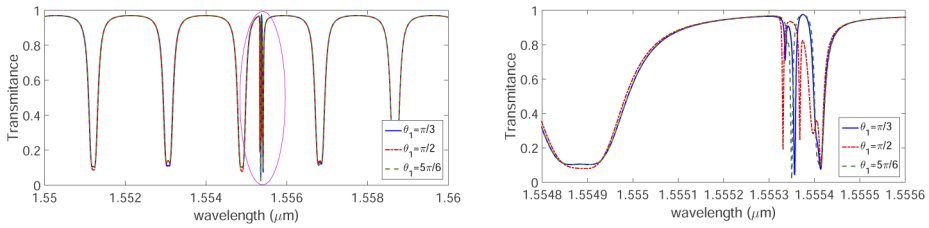

Fig. 7. The normalized transmission spectrum (a) of the double disk coupled to a MRR, the positional angle of the upper disk, θ_1 is taken as parameter while $\theta_3 = \pi/2$. (b) the zoomed view of side resonance(s) for 1.5548 $\mu m < \lambda < 1.15556$ μm. Varying θ_1(and θ_3) affect the properties of the resonance features.

As it is clear in Fig. 7, the variation in θ affects the resonance properties and theoretically, this would allow us to achieve a sharp resonance feature, even in devices which suffer from internal reflections. For the case at hand, the resonance Q-factor is still 7.773×10^5 and its ER is 20.1 dB, same as in the zero-reflection case. Since the output power of the device is highly sensitive to the optical distance between the two disks and obviously they cannot be displaced after fabrication, another tuning mechanism is required. In order to control the optical path between the two disks, we can implement a phase shifter the straight waveguide of the racetrack MRR, as depicted in Fig. 8(a). The phase shifter's operational principle may rely on a simple thermo-optic effect [41]. When the effective index of the phase shifter varies by Δn_{PS}, the resonance wavelength of the

Optics EXPRESS

MRR will drift by $\Delta\lambda$, according to [3,22]:

$$\frac{\Delta\lambda}{\lambda_0} = \frac{\Delta n_{PS} L_{PS}}{n_g L_{PS} + n_{eff}(L_{Ring} - L_{PS})} \tag{8}$$

where λ_0 and n_0 are the resonance wavelength and effective index of the MRR, respectively, at their original state. L_{Ring} is the total length of the MRR waveguide, while L_{PS} is the length of the phase shifter.

Furthermore, the refractive indices of the disks, may be modified either thermally [42] or by pumping light on the disks [34,43]. It is also possible to form a p-i-n diode (especially vertical junction) by doping the disks and tuning the resonance by applying a control voltage [35,36].

In Fig. 8, we show the tuning map for $n_{PS} \pm \Delta n_{PS}$ and $n_{Disk} \pm \Delta n_D$, which allows us to tune the structure for highest possible values of ER, Q and the lowest possible value of FWHM. The sweeping range of n_{PS}, Δn_{PS}, is chosen to be equal to $\Delta n_{PS}/n_g = 0.285\%$ which leads to a 0 to 2π phase-shift, $\Delta\phi$, in λ_{Res}. Δn_{Disk} is set to 10^{-4}. Shifting resonance wavelength, λ_{Res}, by a small change in n_{Disk}, as well as sharp variations in FWHM is a promising feature of this device when employed to act as a high-speed modulator.

When λ_{Res} of the MRR is far away from that of the disk, the interaction between the two will be negligible. However, when the resonance of MRR approached that of the disks, a high-Q resonance with acceptable ER appears in the spectrum with acceptable ER. As can be seen in Fig. 8(c) and 8(d), ER and FWHM experience rather large variation: 5< ER <27 dB and 1.2×10^{-3}< FWHM <5.8×10^{-3} nm by changing total variation of phase shifter, $\Delta\phi$, from 0 to 1.52π. Comparing with 0.148< FWHM <0.185 nm for an identical single MRR, when $\Delta\phi$ is varying from 0 to 2π, the tuning range of FWHM in this design is 4× higher than a simple MRR with the same dimensions, by 0.76× lower $\Delta\phi$. A smaller FWHM is obtained for the case with higher Q ($Q = \lambda_{Res}/FWHM$). An FWHM equal to 2×10^{-3} nm at $\lambda_{Res} = 1555$ nm leads to a Q-factor of approximately 8×10^5. We conclude that by using a simple phase shifter on one of the MRR arms and varying the refractive index of disk, the proposed design can offer

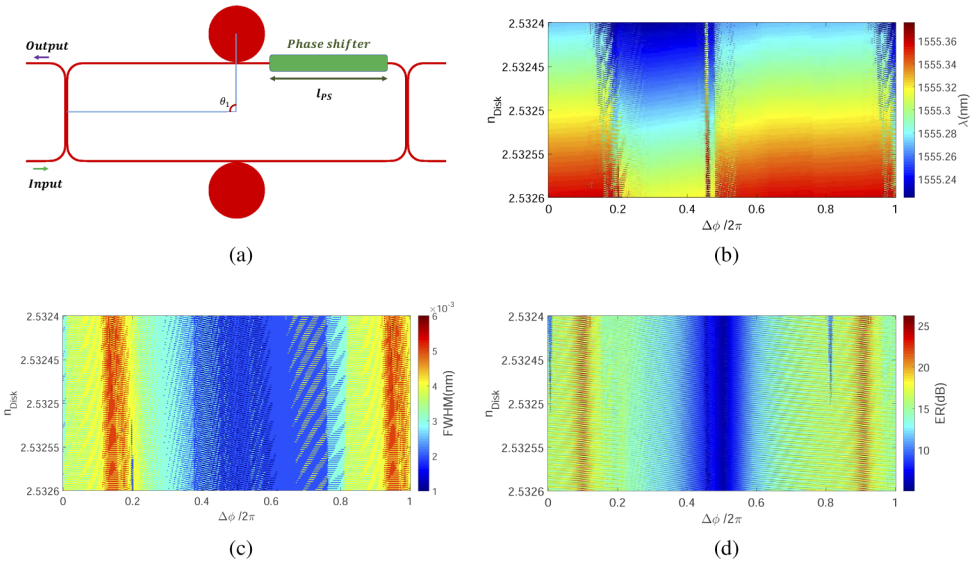

Fig. 8. (a) Using a phase shifter on one of the MRR arm, (b-d) Tuning maps for n_{PS} and n_{Disk}, the effective indices of phase shifter and disks, respectively, to achieve the desired values for resonance wavelength, FWHM and ER when the phase of the phase shifter is varied from 0 to 2π

Optics EXPRESS

a high tunability, a capability which conveniently implemented for a variety of applications. Additionally, it has been shown that we can tune the device simply to achieve a high-Q Fano-like resonance while its ER is kept high. Furthermore, it has been shown that the wavelength of this high-Q resonance is very sensitive to n_{Disk} variation, which makes it a proper candidate for sensing or switching applications.

The specifications of the proposed disk-loaded silicon MRR are summarized in Table 2 and compared with those of the other Fano-like ring resonator recently published in the literature. Present design not only provides an improved slope rate, but also requires a very simple structure compared to the other structures reported in Table 2.

Table 2. Comparison with other reported Fano-like ring resonator

Ref.	structure	R (μm)	ER (dB)	slope rate (dB/nm)	λ_{res} (nm)	Tunable?
[19]	grating waveguide	16.2	22.54	250.4	1564.5	Yes/ high power pumping
[21]	Air-hole in bus-waveguide	30	20	400	1548.5	No
[18][a]	All-grating racetrack resonator	2×10	18.1	72.4	1545	No / used as a sensor
[44]	MRR and a U-bend feedback coupled waveguide	10	30.8	226.5	1555.3	Yes/ phase shifter on U-bend waveguide
[45]	MRR coupled to MZI	60	20	574.6	3810	No
[46]	MZI added to MRR	200 (armlength)	36	700	1550.8	Yes / Heater
[47]	MZI assisted Bragg grating-MR coupled resonant	10	27.4	-	1538	Yes/ Thermally
This work	Disk-loaded MRR	47.25	26.7	880	1555.02	Yes/ Phase shifter

[a]Theoretical study

5. Fabrication and measurement

5.1. SOI implementation

In order to achieve accurate parameters needed for the circuit-level modelling, and to assess the performance of the disk-loaded MRR as a high-Q resonator, we have extracted the model parameters directly from several measurements on the fabricated devices. The devices were fabricated using electron beam lithography (EBL) and inductively coupled plasma etching (ICP) in the Australian Silicon Photonics prototyping service at RMIT Melbourne. For more details of fabrication setup and prototype server the readers can refer to [48]. The same fabrication service has been exploited in [49,50].

The patterning of the resonator was carried out on a 220 nm thick SOI wafer as the substrate. Figure 9(a) shows the schematic design of the structure and Fig. 9(b) depicts the scanning electron

Optics EXPRESS

microscope (SEM) image of the fabricated device. Instead of a circular ring, we designed the MRR as a rounded rectangle, and the positional angles θ_i are recalculated as positions along the rectangular circumference. The waveguide strips have an air-cladding on the top and at the sides. The racetrack geometry of the MRR has a perimeter of 296.88 μm, which corresponds to a 47.25 μm radius of its equivalent circular ring. All waveguides have the same cross-sectional height of 220 nm and widths of 450 nm to ensure single mode operation of the MRR and bus waveguides. The disks were made of silicon, and have a radius of 9.775 μm and the same height of 220 nm. Two grating couplers are fabricated for coupling light into and out of the circuit [51]. Two circuits were fabricated differing only in the coupling gap distance between the ring and the disk, d_2. For the first circuit $d_2 = 300$ nm and for the second $d_2 = 60$ nm.

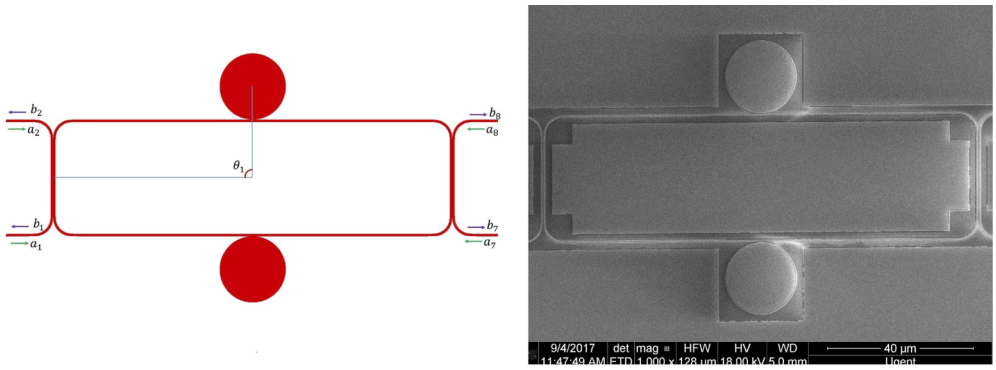

(a) (b)

Fig. 9. (a) Schematic design of the disk-loaded MRR, (b) SEM image of the fabricated device.

Understanding the tuning mechanism required further investigations.

5.2. Measurement results and parameter extraction

The measurements were carried out in the Photonics Research Lab at Ghent University. The characterization of the disk-loaded MRR is performed using the setup shown in Fig. 10. An Agilent 8163B tunable laser with 1 pm wavelength step size is used as the source. Movable stage and movable fiber are used to adjust the input and output power to the device under test [52]. Based on the data obtained from separate measurements of reference circuits, each grating coupler has an insertion loss of around 6 dB, near the measurement wavelength. The similar setup has been used and explained in more details in [53,54]. We have implemented the multi-parameter extraction algorithm, introduced in [55], to fit the experimental data to the circuit-model [56]. Figure 11 compares the measurement and simulation results for the two fabricated disk-loaded MRRs. As can be seen, the simulation results predict transmission spectrum of the disk-loaded MRR with good accuracy. The simulation results were obtained by utilizing optimized model parameters (shown by red-dotted curve in Fig. 11), and fitting the data to the experimental results for the two cases, outlined in Table 3. Note that it is not possible in such a large ring to extract the exact value of the effective index n_{eff}, as the uncertainty on the resonance order is high. Following the method described in [32], we estimated the resonance order of the ring between $m = 430$ and $m = 470$, which results in a series of discrete solutions for n_{eff} with a total uncertainty of $\delta n_{eff} = 0.1$. If assuming a known value for L_{Disk} ($L_{Disk} = 61.42$ μm), the resonance order of the disk is estimated from $m = 97$ to $m = 103$, which means a total uncertainty of effective index of disk is $\delta n_{eff} = 0.075$.

The measurement and simulation results for the first circuit are shown in Fig. 11(a), where the coupling gap between the MRR and the disk, d_2, is assumed to be 300 nm. This large gap results

Optics EXPRESS

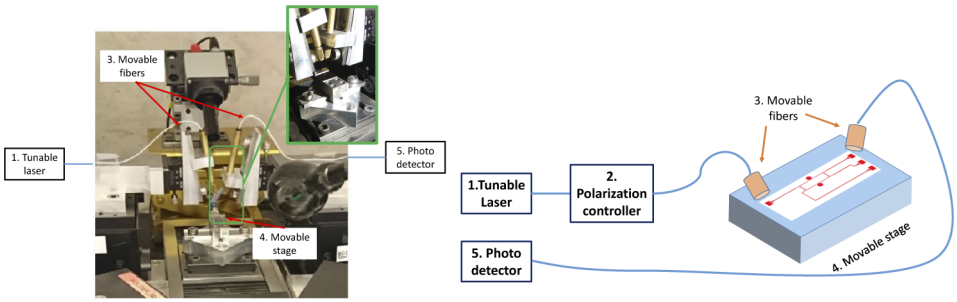

(a) (b)

Fig. 10. Setup to characterize the linear-passive behavior of the device under test (DUT).

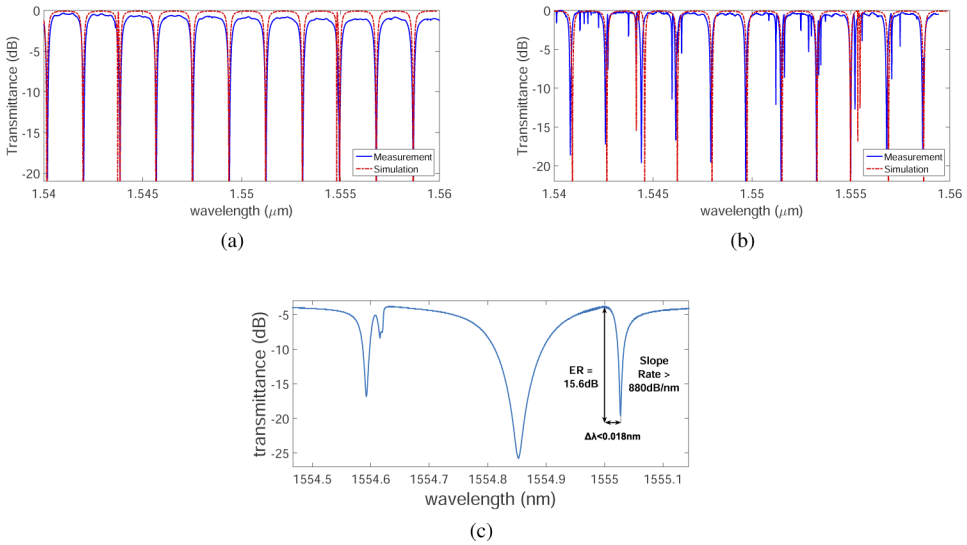

(a) (b)

(c)

Fig. 11. The normalized transmission spectrum obtained from measurement (solid line) and those obtained from the circuit model (dashed line) (a) circuit A, $d_2 = 300\ nm$, (b) circuit B, $d_2 = 60\ nm$, (c) Zoomed view of the high-Q resonance.

Table 3. Extracted parameters obtained by fitting the simulation results to the measurement data at $\lambda_{Res} = 1555\ nm$

Extracted parameters for	κ_{Disk}	$n_{eff_{MRR}}$	$n_{g_{MRR}}$	$n_{eff_{Disk}}$	$n_{g_{Disk}}$
circuit A	0.05	2.36 ± 0.1	4.3644	2.53 ± 0.075	3.5309
circuit B	0.2	2.36 ± 0.1	4.5592	2.53 ± 0.075	3.5312

Optics EXPRESS

in a small coupling coefficient between the MRR and the disk. Nevertheless, the gap is still tight enough to allow for a high-Q resonance, albeit with a small ER.

Figure 11(b) depicts the measurement and simulation results for the second circuit, where $d_2 = 60\ nm$. A smaller d_2 allows for increased the coupling between the MRR and the disks. This clarifies the effect of having two disks. A zoomed view of Fig. 11(b) is shown in Fig. 11(c). Note that a high-Q resonance develops in this case. The slope rate for this resonance is more than 880 nm/dB. This resonance is the result of the interaction between the MRR and the disks resonances. As it is notable in Fig. 11(c), this high-Q resonance has an asymmetric, Fano-like lineshape, while the ER is kept at more than 15 dB. For the second circuit we find that, not only the first mode, but also the higher-radial-order modes of the disk are excited, and this generates extra harmonics in the transmission spectrum. Furthermore, any unwanted defect in the coupling region, such as those originating during fabrication, can lead to unexpected resonance responses, even though they may not have any significant impact on the device performance. We can notice these extra resonances in the transmitted spectrum, shown in Fig. 11(b) and more clearly in Fig. 11(c) which is centered at 1554.8 nm.

Table 3 provides the extracted parameters. As expected, the effective index of disk is higher than that of the MRR, since its radius is smaller. Additionally, the effective indices of the MRR and the disk vary slightly when the coupling gap between the MRR and the disk is varied.

6. Conclusion

A simple structure consisting of a silicon ring and two disks is proposed which can provide a high-Q resonance. A systematic procedure for the design of such MRRs has been explained. The design offers a high tuning efficiency by varying the optical path between two disks, which can be utilized to achieve maximum values of ER and Q simultaneously, thus the design can readily be tailored for a specific application. The advantages of this design include low fabrication cost and its compatibility with the standard CMOS technology.

Acknowledgements. The authors would like to acknowledge Australian Silicon Photonics (www.siliconphotonics.com.au) for the e-beam fabrication of the chip.

Disclosures. The authors declare that there are no conflicts of interest related to this article.

Data availability. Data underlying the results presented in this paper are not publicly available at this time but maybe obtained from the authors upon reasonable request.

References

1. D. Marpaung, J. Yao, and J. Capmany, "Integrated microwave photonics," Nat. Photonics **13**(2), 80–90 (2019).
2. B. Wang, Q. Huang, K. Chen, J. Zhang, G. Kurczveil, D. Liang, S. Palermo, M. R. Tan, R. G. Beausoleil, and S. He, "Modulation on silicon for datacom: Past, present, and future (invited review)," Prog. Electromagn. Res. **166**, 119–145 (2019).
3. W. Bogaerts, P. De Heyn, T. Van Vaerenbergh, K. De Vos, S. Kumar Selvaraja, T. Claes, P. Dumon, P. Bienstman, D. Van Thourhout, and R. Baets, "Silicon microring resonators," Laser Photonics Rev. **6**(1), 47–73 (2012).
4. S. Feng, T. Lei, H. Chen, H. Cai, X. Luo, and A. W. Poon, "Silicon photonics: from a microresonator perspective," Laser Photonics Rev. **6**(2), 145–177 (2012).
5. A. Li, T. Van Vaerenbergh, P. De Heyn, P. Bienstman, and W. Bogaerts, "Backscattering in silicon microring resonators: a quantitative analysis," Laser Photonics Rev. **10**(3), 420–431 (2016).
6. D. Liu, C. Zhang, D. Liang, and D. Dai, "Submicron-resonator-based add-drop optical filter with an ultra-large free spectral range," Opt. Express **27**(2), 416–422 (2019).
7. M. C. Souza, L. A. Barea, F. Vallini, G. F. Rezende, G. S. Wiederhecker, and N. C. Frateschi, "Embedded coupled microrings with high-finesse and close-spaced resonances for optical signal processing," Opt. Express **22**(9), 10430–10438 (2014).
8. S. Pal and S. Gupta, "Performance analysis of an electrostatic doping assisted silicon microring modulator," Opt. Commun. **430**, 131–138 (2019).
9. N. Li, M. Xin, Z. Su, E. S. Magden, N. Singh, J. Notaros, E. Timurdogan, P. Purnawirman, J. D. Bradley, and M. R. Watts, "A silicon photonic data link with a monolithic erbium-doped laser," Sci. Rep. **10**(1), 1–9 (2020).
10. H. Gevorgyan, A. Khilo, Y. Ehrlichman, and M. A. Popović, "Triply resonant coupled-cavity electro-optic modulators for rf to optical signal conversion," Opt. Express **28**(1), 788–815 (2020).

Optics EXPRESS

11. L. Y. Mario, S. Darmawan, and M. K. Chin, "Asymmetric fano resonance and bistability for high extinction ratio, large modulation depth, and low power switching," Opt. Express **14**(26), 12770–12781 (2006).
12. A. Van Rees, Y. Fan, D. Geskus, E. J. Klein, R. M. Oldenbeuving, P. J. Van Der Slot, and K.-J. Boller, "Ring resonator enhanced mode-hop-free wavelength tuning of an integrated extended-cavity laser," Opt. Express **28**(4), 5669–5683 (2020).
13. N. Wu and L. Xia, "High-q and high-sensitivity multi-hole slot microring resonator and its sensing performance," Phys. Scr. **94**(11), 115512 (2019).
14. M. Á. Guillén-Torres, K. Murray, H. Yun, M. Caverley, E. Cretu, L. Chrostowski, and N. A. Jaeger, "Effects of backscattering in high-q, large-area silicon-on-insulator ring resonators," Opt. Lett. **41**(7), 1538–1541 (2016).
15. N. Acharyya and G. Kozyreff, "Large q factor with very small whispering-gallery-mode resonators," Phys. Rev. Appl. **12**(1), 014060 (2019).
16. J. Zhang, X. Leroux, E. Dura'n-Valdeiglesias, C. Alonso-Ramos, D. Marris-Morini, L. Vivien, S. He, and E. Cassan, "Generating fano resonances in a single-waveguide silicon nanobeam cavity for efficient electro-optical modulation," ACS Photonics **5**(11), 4229–4237 (2018).
17. M. F. Limonov, M. V. Rybin, A. N. Poddubny, and Y. S. Kivshar, "Fano resonances in photonics," Nat. Photonics **11**(9), 543–554 (2017).
18. Y. Wen, Y. Sun, C. Deng, L. Huang, G. Hu, B. Yun, R. Zhang, and C. Cui, "High sensitivity and FOM refractive index sensing based on Fano resonance in all-grating racetrack resonators," Opt. Commun. **446**, 141–146 (2016).
19. W. Zhang, W. Li, and J. Yao, "Optically tunable fano resonance in a grating-based fabry–perot cavity-coupled microring resonator on a silicon chip," Opt. Lett. **41**(11), 2474–2477 (2016).
20. G. Yuan, S. Cao, P. Zhang, F. Peng, Z. Peng, and Z. Wang, "Achieving wide-range photonics applications based on a compact grating-assisted silicon micro-ring resonator," Optik **183**, 887–896 (2019).
21. L. Gu, L. Fang, H. Fang, J. Li, J. Zheng, J. Zhao, Q. Zhao, and X. Gan, "Fano resonance lineshapes in a waveguide-microring structure enabled by an air-hole," APL Photonics **5**(1), 016108 (2020).
22. A. Li, Q. Huang, and W. Bogaerts, "Design of a single all-silicon ring resonator with a 150 nm free spectral range and a 100 nm tuning range around 1550 nm," Photonics Res. **4**(2), 84–92 (2016).
23. A. Li and W. Bogaerts, "Using backscattering and backcoupling in silicon ring resonators as a new degree of design freedom," Laser Photonics Rev. **13**, 1800244 (2019).
24. O. Schwelb and I. Frigyes, "All-optical tunable filters built with discontinuity-assisted ring resonators," J. Lightwave Technol. **19**(3), 380–386 (2001).
25. Z. Zhang, M. Dainese, L. Wosinski, and M. Qiu, "Resonance-splitting and enhanced notch depth in soi ring resonators with mutual mode coupling," Opt. Express **16**(7), 4621–4630 (2008).
26. W. Kim, Ş. K. Özdemir, J. Zhu, L. He, and L. Yang, "Demonstration of mode splitting in an optical microcavity in aqueous environment," Appl. Phys. Lett. **97**(7), 071111 (2010).
27. R. Haldar, S. Das, and S. K. Varshney, "Theory and design of off-axis microring resonators for high-density on-chip photonic applications," J. Lightwave Technol. **31**(24), 3976–3986 (2013).
28. M. Bahadoran, J. Ali, and P. P. Yupapin, "Ultrafast all-optical switching using signal flow graph for panda resonator," Appl. Opt. **52**(12), 2866–2873 (2013).
29. J. Čtyrokỳ, I. Richter, and M. Šiňor, "Dual resonance in a waveguide-coupled ring microresonator," Opt. Quantum Electron. **38**(9-11), 781–797 (2007).
30. X. Chen, P. Stroobant, M. Pickavet, and W. Bogaerts, "Graph representations for programmable photonic circuits," J. Lightwave Technol. **38**(15), 4009–4018 (2020).
31. D. M. Pozar, *Microwave engineering* (John wiley & sons, 2009).
32. Y. Xing, J. Dong, S. Dwivedi, U. Khan, and W. Bogaerts, "Accurate extraction of fabricated geometry using optical measurement," Photonics Res. **6**(11), 1008–1020 (2018).
33. R. Dekker, N. Usechak, M. Först, and A. Driessen, "Ultrafast nonlinear all-optical processes in silicon-on-insulator waveguides," J. Phys. D: Appl. Phys. **40**(14), R249–R271 (2007).
34. V. R. Almeida, C. A. Barrios, R. R. Panepucci, and M. Lipson, "All-optical control of light on a silicon chip," Nature **431**(7012), 1081–1084 (2004).
35. Z. Ying, Z. Wang, Z. Zhao, S. Dhar, D. Z. Pan, R. Soref, and R. T. Chen, "Comparison of microrings and microdisks for high-speed optical modulation in silicon photonics," Appl. Phys. Lett. **112**(11), 111108 (2018).
36. D. Gostimirovic, F. De Leonardis, R. Soref, V. M. Passaro, and N. Y. Winnie, "Ultrafast electro-optical disk modulators for logic, communications, optical repeaters, and wavelength converters," Opt. Express **28**(17), 24874–24888 (2020).
37. P. Ma, H. Jäckel, G.-L. Bona, and C. Hafner, "Ultrafast, compact, and energy efficient all-optical switches based on a saturable absorbing cavity," IEEE J. Quantum Electron. **50**(7), 568–574 (2014).
38. M. Masi, M. Mancinelli, A. Battarelli, R. Guider, M. R. Vanacharla, P. Bettotti, J.-M. Fedeli, and L. Pavesi, "A silicon photonic interferometric router device based on scissor concept," J. Lightwave Technol. **29**(18), 2747–2753 (2011).
39. M. Tomita, T. Sudo, K. Yoshimura, and D. Sugio, "Development of the pulse peak from peak-truncated gaussian optical pulses in a serial array of high-q ring resonators," Phys. Rev. A **102**(4), 043507 (2020).
40. B. Peng, Ş. K. Özdemir, W. Chen, F. Nori, and L. Yang, "What is and what is not electromagnetically induced transparency in whispering-gallery microcavities," Nat. Commun. **5**(1), 5082 (2014).
41. M. Jacques, A. Samani, E. El-Fiky, D. Patel, Z. Xing, and D. V. Plant, "Optimization of thermo-optic phase-shifter design and mitigation of thermal crosstalk on the soi platform," Opt. Express **27**(8), 10456–10471 (2019).

Optics EXPRESS

42. X. Jiang and L. Yang, "Optothermal dynamics in whispering-gallery microresonators," Light: Sci. Appl. **9**(1), 1–15 (2020).
43. T. Liang, L. Nunes, T. Sakamoto, K. Sasagawa, T. Kawanishi, M. Tsuchiya, G. Priem, D. V. Thourhout, P. Dumon, R. Baets, and H. Tsang, "Ultrafast all-optical switching by cross-absorption modulation in silicon wire waveguides," Opt. Express **13**(19), 7298–7303 (2005).
44. G. Zhao, T. Zhao, H. Xiao, Z. Liu, G. Liu, J. Yang, Z. Ren, J. Bai, and Y. Tian, "Tunable fano resonances based on microring resonator with feedback coupled waveguide," Opt. Express **24**(18), 20187–20195 (2016).
45. B. Troia, J. S. Penades, Z. Qu, A. Z. Khokhar, A. Osman, Y. Wu, C. Stirling, M. Nedeljkovic, V. M. Passaro, and G. Z. Mashanovich, "Silicon ring resonator-coupled mach–zehnder interferometers for the fano resonance in the mid-ir," Appl. Opt. **56**(31), 8769–8776 (2017).
46. A. Li and W. Bogaerts, "An actively controlled silicon ring resonator with a fully tunable fano resonance," APL Photonics **2**(9), 096101 (2017).
47. Z. Zhang, G. I. Ng, T. Hu, H. Qiu, X. Guo, W. Wang, M. S. Rouifed, C. Liu, J. Sia, J. Zhou, C. G. Littlejohns, M. Nedeljkovic, G. T. Reed, and H. Wang, "Experimental demonstration of thermally tunable fano and eit resonances in coupled resonant system on soi platform," IEEE Photonics J. **10**(3), 1–8 (2018).
48. "Australian silicon photonics," https://www.siliconphotonics.com.au.
49. Y. Xing, U. Khan, A. R. Alves Júnior, and W. Bogaerts, "Behavior model for directional coupler," in *Proceedings Symposium IEEE Photonics Society Benelux*, (2017), pp. 128–131.
50. X. Han, Z. Zhang, J. Yang, H. Xiao, G. Ren, Y. Jiang, T. Zhao, T. G. Nguyen, A. Mitchell, J. Yang, and Y. Tian, "On-chip switchable and reconfigurable optical mode exchange device using cascaded three-waveguide-coupling switches," Opt. Express **28**(7), 9552–9562 (2020).
51. D. Vermeulen, Y. De Koninck, Y. Li, E. Lambert, W. Bogaerts, R. Baets, and G. Roelkens, "Reflectionless grating couplers for silicon-on-insulator photonic integrated circuits," Opt. Express **20**(20), 22278–22283 (2012).
52. L. Chrostowski and M. Hochberg, *Silicon photonics design: from devices to systems* (Cambridge University Press, 2015).
53. A. Li and W. Bogaerts, "Reconfigurable nonlinear nonreciprocal transmission in a silicon photonic integrated circuit," Optica **7**(1), 7–14 (2020).
54. Y. Xing, "Behavioural models, parameter extraction and yield prediction for silicon photonic circuits," Ph.D. thesis, Ghent University (2019).
55. A. Ruocco, M. Fiers, M. Vanslembrouck, T. Van Vaerenbergh, and W. Bogaerts, "Multi-parameter extraction from soi photonic integrated circuits using circuit simulation and evolutionary algorithms," Proc. SPIE **9366**, 936606 (2015).
56. S. Dwivedi, A. Ruocco, M. Vanslembrouck, T. Spuesens, P. Bienstman, P. Dumon, T. Van Vaerenbergh, and W. Bogaerts, "Experimental extraction of effective refractive index and thermo-optic coefficients of silicon-on-insulator waveguides using interferometers," J. Lightwave Technol. **33**(21), 4471–4477 (2015).